Available online at www.sciencedirect.com
SCIENCE DIRECT®
Journal of Computational Physics 195 (2004) 629–654
JOURNAL OF COMPUTATIONAL PHYSICS
www.elsevier.com/locate/jcp

Unified formulation for compressible and incompressible flows by using multi-integrated moments I: one-dimensional inviscid compressible flow

Feng Xiao *

Department of Energy Sciences, Tokyo Institute of Technology, 4259 Nagatsuta, Midori-ku, Yokohama 226-8502, Japan

Received 11 April 2003; received in revised form 5 August 2003; accepted 2 October 2003

Abstract

This paper presents a novel numerical formulation for computing flows of any Mach number. The following features make the present scheme different from the existing works: (1) The spatial discretizations are constructed by using two kinds of moments which are defined as the volume integrated average (VIA) and the surface integrated average (SIA), both of which are computed as the prognostic variables; (2) the CIP-CSL3 (constrained interpolation profile-conservative semi-lagrangian with third-order polynomial function) scheme is used for the advection transport; (3) a simple artificial compression can be devised by modifying the slope parameter in the CIP-CSL3 scheme. Moreover, the conservation is exactly assured for the VIA quantities. As the first of the series, this paper mainly focuses on the computations of inviscid compressible flows. Our numerical results show that the present method gives correct shock speed, well-resolved shock front, contact discontinuity and rarefaction waves for a wide spectrum of test problems.

AMS: 65C20; 76M20; 76T05; 65P05; 77F05

Keywords: Unified method; Conservative scheme; Integrated moment; Pressure projection; Euler conservation laws; Shock capturing; Compressible and incompressible flows

1. Introduction

A unified method which appears accurate and efficient for all Mach number, ranging from zero to supersonic is attractive for practical applications. The standard methods for compressible flows show to be not numerically robust and efficient in the case of low Mach number or weak compressibility, because of the stiffness of the governing equations. A remedy that makes the numerical methods for compressible flows

* Tel.: +81-45-924-5538; fax: +81-45-924-5538.
E-mail address: xiao@es.titech.ac.jp (F. Xiao).

0021-9991/$ - see front matter
doi:10.1016/j.jcp.2003.10.014

applicable to flows of low Mach number is to precondition the original system, see [5,15,24,27], for details on this category.

The alternative to this is to extend the projection type methods for incompressible flows by introducing the compressibility into the projection procedure. Originated by Harlow and coworkers [6–8] and Chorin [4], the classical method for incompressible flows is to project the final velocity onto a divergence free subspace. The pressure or pressure-equivalent variable plays a central role in the projection method. Since the change in pressure is of much more physical significance than that in density under weak compressibility, the projection methodology (often referred also as pressure based method) is more stable and efficient in the computations for low Mach number flows. The pressure based projection methods in fact suggest an implicit treatment for the acoustic wave related part in the governing equation, thus some stable numerical formulations that belong to the pressure based methods for incompressible flow can be extended to compressible flows by including the compressibility into the projection procedure. Researches in this direction have been conducted in [3,12,14,18,22,38]. A more complete review can be found in [28]. In these works, a staggered grid which proves to be more suitable for coupling the velocity and pressure in a projection method has been adopted, and some of them are not cast in a conservative form. The numerical results for compressible flows of this sort algorithms can be competitive to the conventional compressible flow solvers in some situations, however further improvements are still required concerning both spatial approximations and time stepping algorithms.

This paper presents a unified scheme for compressible and incompressible flows which is different from the existing ones. We solve the conservation laws for all the mass, the momentum and the total energy through a fractional step procedure with the pressure been pre-diagnosed by a Poisson equation derived from the mass continuity equation, the momentum equation, the equation of state and the thermodynamic equation to include the compressibility. The spatial discretization and the time marching are approximated by a multi-integrated moment method recently proposed by the author [31]. Two integrated moments of a physical quantity are defined as the volume integrated average (VIA) and the surface integrated average (SIA). The resulting methodology, which is called VSIAM3 (volume/surface integrated average based multi-moment method), applies to general dynamical problems defined in time-space domain. The integrated moments which are hierarchically defined in different dimensionality are reciprocal in constructing numerical model. The VSIAM3 conserves the VIA quantities which are computed via a flux form. The advection transport is computed by CIP-CSL3 (constrained interpolation profile-conservative semi-lagrangian with third-order polynomial function) scheme [33], which provides straightforwardly an artificial compression parameter to reduce the numerical diffusions.

In Section 2, the numerical formulation is described. Numerical tests are given in Section 3. Since the present method is derived from an incompressible framework, it is trivial to implement it to incompressible flows. To see if such a pressure based method works well with compressible flows, we extensively tested the scheme with various typical benchmark tests of compressible flow in this paper. Comparisons with other existing methods were also carried out. The paper ends with some short remarks in Section 4.

2. The numerical formulation

We consider the inviscid compressible flow. The Euler equations describe the non-linear hyperbolic system for the dynamics of inviscid compressible flow. Its conservative form is written as

$$\frac{\partial \mathbf{U}}{\partial t} + \frac{\partial \mathbf{F}(\mathbf{U})}{\partial x} = 0, \tag{1}$$

where

$$\mathbf{U} = \begin{pmatrix} \rho \\ m \\ E \end{pmatrix}$$

and

$$\mathbf{F}(\mathbf{U}) = \begin{pmatrix} m \\ um + p \\ Eu + pu \end{pmatrix},$$

with ρ being the density, u the velocity, $m = \rho u$ the momentum and E the total energy. Suppose we have perfect gas, the pressure can be obtained by the equation of state as $p = (E - \rho u^2/2)(\gamma - 1)$ with γ being the ratio of the specific heats. The flux in Eq. (1) is further divided into the advection part and the non-advection part,

$$\mathbf{F}(\mathbf{U}) = \mathbf{F}_{\mathrm{I}}(\mathbf{U}) + \mathbf{F}_{\mathrm{II}}(\mathbf{U}) = \begin{pmatrix} m \\ um \\ Eu \end{pmatrix} + \begin{pmatrix} 0 \\ p \\ pu \end{pmatrix}.$$

2.1. The fractional step procedure

Let us start with all values at nth step known as ρ^n, m^n and E^n. We first compute the advection part, denoted by $\mathbf{F}_{\mathrm{I}}(\mathbf{U})$, with the CSL3 scheme, which is going to be described later, and obtain the value for density at the new time step ρ^{n+1} and the provisional values of the momentum and the total energy as $m^{\diamondsuit}$ and $E^{\diamondsuit}$. The semi-discretized equations of the non-advection part are then written as

$$\frac{m^{n+1} - m^{\diamondsuit}}{\Delta t} = -\frac{\partial p^{n+1}}{\partial x} \tag{2}$$

and

$$\frac{E^{n+1} - E^{\diamondsuit}}{\Delta t} = -\frac{\partial (up)^{n+1}}{\partial x}, \tag{3}$$

where Δt is the time integration interval. From (2), we have

$$\frac{1}{\Delta t}\left(\frac{\partial m^{n+1}}{\partial x} - \frac{\partial m^{\diamondsuit}}{\partial x}\right) = -\frac{\partial^2 p^{n+1}}{\partial x^2}. \tag{4}$$

The first term on the left-hand side of Eq. (4) provides a point to include the compressibility into a pressure based projection method, and is approximated by

$$\frac{\partial m^{n+1}}{\partial x} = u^{\diamondsuit}\frac{\partial \rho^{n+1}}{\partial x} + \rho^{n+1}\frac{\partial u^{n+1}}{\partial x}. \tag{5}$$

For compressible flow, change in fluid density connects directly to the volume change rate, hence to the divergence which is then expressed through the spatial variations in velocity. This is presented by the following equation in 1D:

$$\frac{\delta \rho}{\delta t} = -\rho\frac{\delta u}{\delta x}, \tag{6}$$

where $\delta/\delta t$ and $\delta/\delta x$ denote the variations in time and space, respectively, for a fluid parcel.

Recall the equation of state and the first law of thermodynamics, we have the following relations among the thermodynamic variables and the velocity field,

$$\frac{\delta p}{\delta t} = (\gamma - 1)\left(e\frac{\delta \rho}{\delta t} + \rho\frac{\delta e}{\delta t}\right) \tag{7}$$

and

$$\frac{\delta e}{\delta t} = -\frac{p}{\rho}\frac{\delta u}{\delta x}. \tag{8}$$

Eqs. (6), (7) and (8) are the part that relates to the acoustic wave and compressibility. We then arrive at

$$\frac{\delta u}{\delta x} = -\frac{1}{\gamma p}\frac{\delta p}{\delta t}. \tag{9}$$

The above relation states the response of the velocity field to the disturbance in the pressure field or vice versa.

By replacing the divergence term expressed by (9) in (5) and using Euler forward stepping to the pressure tendency, we recast (4) as

$$\frac{\partial^2 p^{n+1}}{\partial x^2} = \frac{1}{\Delta t}\left(-u^{\diamondsuit}\frac{\partial \rho^{n+1}}{\partial x} + \frac{1}{C^2}\frac{p^{n+1} - p^{\diamondsuit}}{\Delta t} + \frac{\partial m^{\diamondsuit}}{\partial x}\right), \tag{10}$$

where $C = \sqrt{\gamma p^{\diamondsuit}/\rho^{n+1}}$ is the sound speed. It is obvious that Eq. (10) becomes exactly the pressure Poisson equation in the projection method for incompressible flows when Mach number ($M = u/C$) approaches zero, and we do not meet the singularity in the pressure Poisson equation in the case of $M = 0$. The above Poisson equation is similar to those in the ICE (implicit continuous Eulerian) method [7] and the PISO (pressure implicit with splitting of operators) [11] method, but we use a fractional step procedure. This make the computation very simple, though leading to a first-order time stepping.

As we will see later, the multi-moment framework provides a convenient discretization for Eq. (10) where the averaging due to the conventional staggered grid is not needed.

Our numerical experiments show that competitive results can be obtained even with the following simple formula for the compressible regime

$$p^{n+1} = C^2\Delta t\left(u^{\diamondsuit}\frac{\partial \rho^{n+1}}{\partial x} + \frac{\rho^{n+1}}{\gamma \Delta t} - \frac{\partial m^{\diamondsuit}}{\partial x}\right). \tag{11}$$

This equation is obtained by just omitting the second-order derivative of pressure in Eq. (10). Eq.(11) gives a formulation quite similar to the artificial viscosity of Neumann type [10,19,29], i.e., the extra artificial viscosity to the pressure is in proportion to the convergence in velocity field. This reveals to some extent that the pressure computation in the non-advection part can be interpreted as adding an artificial viscosity to the pressure field. Nevertheless, we solve the Poisson equation (10) instead of an explicit artificial viscosity in the present model to get a uniform scheme that also works for low Mach or incompressible flows.

In this study, the Poisson pressure equation (10) is solved by the Thomas algorithm, a direct solver based on LU decomposition. An iterative method might be more efficient in multi-dimensional computations. After p^{n+1} is solved by (10) or (11), the momentum and the total energy are then updated by (2) and (3). It is noted that all the mass, momentum and total energy are predicted in a conservative form, which is different from those reported in [3,38] where all or part of the variables are computed by non-conservative formulations. Using multi-integrated moment, our spatial discretizations for the above equations are com-

pletely different from the conventional finite difference method or finite volume method, and will be discussed next.

2.2. The multi-moment discretization

The multi-moment concept is found in the CIP method [35,36], where in addition to the grid point value of a physical field, the first-order derivatives are also treated as the extra 'moments' and predicted in the numerical model as other dependent variables. The CIP method has been so far improved and applied to various physical problems. See [39] for a review on the CIP method. Utilizing the multi-moments makes the CIP method different from other numerical categories, and provides us a new way to construct numerical formulations. In this paper, instead of the derivative moments, we use two kinds of integrated moments to build the numerical model.

Let $\phi(x_1, x_2, \ldots, x_m, t)$ be any physical variable defined in m dimensional coordinate and time t. We denote a fixed control volume (CV) by $\mathscr{V} \subset \mathscr{R}^m$ and its surface by $\mathscr{S} \subset \mathscr{R}^{m-1}$. In practice, the surface is approximated by a set of L connected planes, i.e., $\mathscr{S} = \cup_{l=1}^{L} \mathscr{S}_l$.

The volume-integrated average (VIA) of $\phi(x_1, x_2, \ldots, x_m, t)$ can be defined as

$$\overline{{}^{V}\phi} = \frac{1}{|\mathscr{V}|} \int_{\mathscr{V}} \phi(x_1, x_2, \ldots, x_m, t)\, \mathrm{d}V \tag{12}$$

and the surface-integrated averages (SIAs) of $\phi(x_1, x_2, \ldots, x_m, t)$ on each segment of the surface planes are computed as

$$\overline{{}^{S_l}\phi} = \frac{1}{|\mathscr{S}_l|} \int_{\mathscr{S}_l} \phi(x_1, x_2, \ldots, x_m, t)\, \mathrm{d}S \quad \text{for } l = 1, 2, \ldots, L, \tag{13}$$

where $|\mathscr{V}|$ and $|\mathscr{S}_l|$ denote the volume of the CV and the area of the lth surface segment.

Choosing the control volume and the surface segments is arbitrary. From practical consideration, the simplest control volume can be a hyper cube in $\mathscr{R}^m$ with all surface segments being, respectively, normal to the coordinate axes. Thus, we have one VIA ($\overline{{}^{V}\phi}$) and m SIAs ($\overline{{}^{S_1}\phi}, \overline{{}^{S_2}\phi}, \ldots, \overline{{}^{S_m}\phi}$) for the physical field $\phi(x_1, x_2, \ldots, x_m, t)$. The VIA $\overline{{}^{V}\phi}$ is defined inside the CV and staggeringly located in respect to the SIAs ($\overline{{}^{S_l}\phi}$, $l = 1, 2, \ldots, m$) which are on the surface segments.

Note that the VIA degrades to a line integrated average and the SIA to a point value in one dimensional case, we denote them by $\overline{{}^{x}\phi}$ and $\overline{{}^{0}\phi}$. Let $\phi(x, t)$ be integrable on the x line which has a partition defined by $\mathscr{P}(X_i) = (x_{i-(1/2)}, x_{i+(1/2)})$ with $i = 1, \ldots, i_{\max}$. We have one VIA and one SIA defined, respectively, as

$$\overline{{}^{x}\phi(t)}_i = \frac{1}{\Delta x_i} \int_{x_{i-(1/2)}}^{x_{i+(1/2)}} \phi(x, t)\, \mathrm{d}x \tag{14}$$

and

$$\overline{{}^{0}\phi(t)}_{i+(1/2)} = \phi(x_{i+(1/2)}, t), \tag{15}$$

with $\Delta x_i = x_{i+(1/2)} - x_{i-(1/2)}$.

The discretizations of the differential or integral operators can be computed by using interpolations based on VIA and SIA. Shown in Fig. 1, a simple linear interpolation can be constructed by using the VIAs of the two neighboring cells as

$$\Phi_1(x) = a_1 + b_1\big(x - x_{i+(1/2)}\big) \tag{16}$$

with

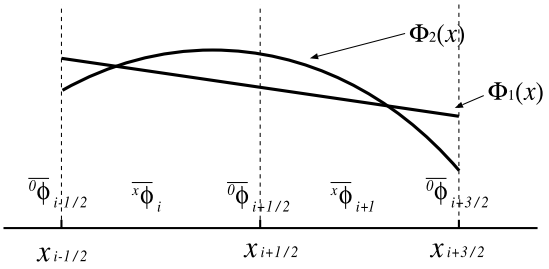

Fig. 1. The mesh and the locations of VIA and SIA in a multi-integrated moment method. $\Phi_1(x)$ and $\Phi_2(x)$ indicate the linear and the parabolic interpolations, respectively, which can be constructed over two cells based on VIA and SIA.

$$a_1 = \frac{1}{\Delta x_i + \Delta x_{i+1}} \left(\Delta x_{i+1} \overline{{}^{x}\phi}_i + \Delta x_i \overline{{}^{x}\phi}_{i+1} \right), \tag{17}$$

$$b_1 = \frac{2}{\Delta x_i + \Delta x_{i+1}} \left(\overline{{}^{x}\phi}_{i+1} - \overline{{}^{x}\phi}_i \right), \tag{18}$$

while a parabolic polynomial can be constructed by using both VIA and SIA as

$$\Phi_2(x) = a_2 + b_2 \left(x - x_{i+(1/2)} \right) + c_2 \left(x - x_{i+(1/2)} \right)^2, \tag{19}$$

where

$$a_2 = \overline{{}^{0}\phi}_{i+(1/2)}, \tag{20}$$

$$b_2 = \frac{2}{\Delta x_i + \Delta x_{i+1}} \left[\frac{\Delta x_i}{\Delta x_{i+1}} \left(\overline{{}^{x}\phi}_{i+1} - \overline{{}^{0}\phi}_{i+(1/2)} \right) - \frac{\Delta x_{i+1}}{\Delta x_i} \left(\overline{{}^{x}\phi}_i - \overline{{}^{0}\phi}_{i+(1/2)} \right) \right], \tag{21}$$

$$c_2 = 3 \left[\frac{1}{\Delta x_i (\Delta x_i + \Delta x_{i+1})} \left(\overline{{}^{x}\phi}_i - \overline{{}^{0}\phi}_{i+(1/2)} \right) + \frac{1}{\Delta x_{i+1} (\Delta x_i + \Delta x_{i+1})} \left(\overline{{}^{x}\phi}_{i+1} - \overline{{}^{0}\phi}_{i+(1/2)} \right) \right]. \tag{22}$$

Similarly, a quartic interpolation can be constructed by including the extra two SIA values, $\overline{{}^{0}\phi}_{i-(1/2)}$ and $\overline{{}^{0}\phi}_{i+(3/2)}$, at $x_{i-(1/2)}$ and $x_{i+(3/2)}$.

The gradient operator, $\partial_x \phi \equiv \partial\phi/\partial x$, at $x_{i+(1/2)}$ then can be computed by

$$\overline{{}^{x}\partial_x \phi}_{i+(1/2)} = \left[\frac{\partial \Phi_1(x)}{\partial x} \right]_{i+(1/2)} = b_1 \tag{23}$$

or

$$\overline{{}^{x}\partial_x \phi}_{i+(1/2)} = \left[\frac{\partial \Phi_2(x)}{\partial x} \right]_{i+(1/2)} = b_2. \tag{24}$$

The Laplacian operator, $\partial_{xx} \phi \equiv \partial^2\phi/\partial x^2$, can be approximated by

$$\overline{{}^{x}\partial_{xx} \phi}_i = \frac{1}{\Delta x_i} \left\{ \left[\frac{\partial \Phi_1(x)}{\partial x} \right]_{i+(1/2)} - \left[\frac{\partial \Phi_1(x)}{\partial x} \right]_{i-(1/2)} \right\} \tag{25}$$

or

$$\overline{{}^{x}\partial_{xx}\phi}_i = \frac{1}{\Delta x_i}\left\{\left[\frac{\partial \Phi_2(x)}{\partial x}\right]_{i+(1/2)} - \left[\frac{\partial \Phi_2(x)}{\partial x}\right]_{i-(1/2)}\right\}. \tag{26}$$

It is obvious that these formulations are exactly equivalent to the central differencing if the mesh is uniformly spaced and the VIA is located at the cell center.

Regarding the Euler equations, given the VIAs and the SIAs at $t = t^n$ as $\overline{{}^{x}\rho}^n$, $\overline{{}^{x}m}^n$, $\overline{{}^{x}E}^n$, $\overline{{}^{0}\rho}^n$, $\overline{{}^{0}m}^n$ and $\overline{{}^{0}E}^n$, we use the CIP-CSL3 scheme to solve the advection part and get $\overline{{}^{x}\rho}^{n+1}$, $\overline{{}^{x}m}^{\diamondsuit}$, $\overline{{}^{x}E}^{\diamondsuit}$, $\overline{{}^{0}\rho}^{n+1}$, $\overline{{}^{0}m}^{\diamondsuit}$ and $\overline{{}^{0}E}^{\diamondsuit}$.

Considering the pressure as a VIA quantity, we have the discretized form for (10)

$$\begin{aligned}&\frac{2}{\Delta x_i}\left(\frac{\overline{{}^{x}p}^{n+1}_{i+1} - \overline{{}^{x}p}^{n+1}_{i}}{\Delta x_i + \Delta x_{i+1}} - \frac{\overline{{}^{x}p}^{n+1}_{i} - \overline{{}^{x}p}^{n+1}_{i-1}}{\Delta x_{i-1} + \Delta x_i}\right) + \frac{1}{(C_i\Delta t)^2}\overline{{}^{x}p}^{n+1}_{i}\\ &\quad = \frac{1}{\Delta t}\left(-\overline{{}^{x}u}^{\diamondsuit}_i \frac{\overline{{}^{0}\rho}^{\diamondsuit}_{i+(1/2)} - \overline{{}^{0}\rho}^{\diamondsuit}_{i-(1/2)}}{\Delta x_i} - \frac{1}{C_i^2}\frac{\overline{{}^{x}p}^{\diamondsuit}_i}{\Delta t} + \frac{\overline{{}^{0}m}^{\diamondsuit}_{i+(1/2)} - \overline{{}^{0}m}^{\diamondsuit}_{i-(1/2)}}{\Delta x_i}\right),\end{aligned} \tag{27}$$

with $\overline{{}^{x}u}^{\diamondsuit}_i = \overline{{}^{x}m}^{\diamondsuit}_i / \overline{{}^{x}\rho}^{n+1}_i$, $C_i = \sqrt{\gamma p_i^{\diamondsuit}/\rho_i^{n+1}}$ and $\overline{{}^{x}p}^{\diamondsuit}_i = [\overline{{}^{x}E}^{\diamondsuit}_i - \overline{{}^{x}\rho}^{n+1}_i(\overline{{}^{x}u}^{\diamondsuit}_i)^2/2](\gamma - 1)$.

Correspondingly, the computational expression for (11) is

$$\overline{{}^{x}p}^{n+1}_i = C_i^2\Delta t\left(\overline{{}^{x}u}^{\diamondsuit}_i \frac{\overline{{}^{0}\rho}^{n+1}_{i+(1/2)} - \overline{{}^{0}\rho}^{n+1}_{i-(1/2)}}{\Delta x_i} + \frac{\overline{{}^{x}\rho}^{n+1}_i}{\gamma\Delta t} - \frac{\overline{{}^{0}m}^{\diamondsuit}_{i+(1/2)} - \overline{{}^{0}m}^{\diamondsuit}_{i-(1/2)}}{\Delta x_i}\right). \tag{28}$$

Once $\overline{{}^{x}p}^{n+1}_i$ is computed for $i = 1, 2, \ldots, i_{\max}$, we predict the SIA quantity for the momentum by

$$\overline{{}^{0}m}^{n+1}_{i+(1/2)} = \overline{{}^{0}m}^{\diamondsuit}_{i+(1/2)} - 2\Delta t\frac{\overline{{}^{x}p}^{n+1}_{i+1} - \overline{{}^{x}p}^{n+1}_{i}}{\Delta x_i + \Delta x_{i+1}}. \tag{29}$$

The VIA of m is then advanced by the so called *time-evolution converting* (TEC) formula

$$\overline{{}^{x}m}^{n+1}_i = \overline{{}^{x}m}^{\diamondsuit}_i + \frac{1}{2}\left(\overline{{}^{0}m}^{n+1}_{i+(1/2)} - \overline{{}^{0}m}^{\diamondsuit}_{i+(1/2)} + \overline{{}^{0}m}^{n+1}_{i-(1/2)} - \overline{{}^{0}m}^{\diamondsuit}_{i-(1/2)}\right). \tag{30}$$

The SIA of the total energy is predicted as

$$\overline{{}^{0}E}^{n+1}_{i+(1/2)} = \overline{{}^{0}E}^{\diamondsuit}_{i+(1/2)} - 2\Delta t\frac{\overline{{}^{x}u}^{n+1}_{i+1}\overline{{}^{x}p}^{n+1}_{i+1} - \overline{{}^{x}u}^{n+1}_{i}\overline{{}^{x}p}^{n+1}_{i}}{\Delta x_i + \Delta x_{i+1}}. \tag{31}$$

Analogously, the VIA of E is finally updated by the corresponding TEC formula

$$\overline{{}^{x}E}^{n+1}_i = \overline{{}^{x}E}^{\diamondsuit}_i + \frac{1}{2}\left(\overline{{}^{0}E}^{n+1}_{i+(1/2)} - \overline{{}^{0}E}^{\diamondsuit}_{i+(1/2)} + \overline{{}^{0}E}^{n+1}_{i-(1/2)} - \overline{{}^{0}E}^{\diamondsuit}_{i-(1/2)}\right). \tag{32}$$

An alternative to (31) and (32) for updating the total energy is to compute the VIA of E by an upwind formulation in terms of the VIAs of p and u at first, and then update the SIA of E via the TEC formula. This gives a convenient discretization in multi-dimensional computations.

2.3. The CIP_CSL3 scheme

In the solution procedure discussed in the above subsection, the advection phase can be computed by the so called Constrained Interpolation Profile_Conservative Semi-Lagrangian (CIP_CSL) schemes [33,37]. In

the present study, we used the CIP_CSL3 scheme proposed in [33]. In CIP_CSL3 scheme, the numerical oscillations were eliminated by introducing a slope limiter at the center of each mesh cell. The slope, as a parameter in reconstructing the interpolation profile, in fact provides us a large freedom to control the interpolation profile and thus to modify the numerical solutions. It has been used in an interface tracking scheme for incompressible flow [32] and also appears effective in reducing numerical diffusions in compressible flow simulations. Next, we briefly describe the CIP-CSL3 scheme in terms of the two integrated moments, VIA and SIA.

The CIP-CSL3 method is originally designed to solve the transport equation

$$\frac{\partial \phi}{\partial t} + \frac{\partial}{\partial x}(u\phi) = 0, \tag{33}$$

where t refers to the time, x the spatial coordinate, u the advection speed and ϕ the transported quantity.

Let ${}^{x}\overline{\phi}_i^n$ and ${}^{0}\overline{\phi}_{i+(1/2)}^n$, with $i = 1, 2, \ldots, i_{\max}$, be the VIA and the SIA of ϕ defined by (14) and (15), respectively. The ith piece of the interpolation function is constructed over upwind stencils. Taking the case of $u < 0$, a left-bias interpolation can be written as

$$\Phi_i^{\mathrm{L}}(x) = {}^{0}\overline{\phi}_{i-(1/2)}^n + c_{1i}^{\mathrm{L}}\left(x - x_{i-(1/2)}\right) + c_{2i}^{\mathrm{L}}\left(x - x_{i-(1/2)}\right)^2 + c_{3i}^{\mathrm{L}}\left(x - x_{i-(1/2)}\right)^3, \quad \text{for} \quad x \in \left[x_{i-(1/2)}, x_{i+(1/2)}\right]. \tag{34}$$

From the continuity conditions of $\Phi_i^{\mathrm{L}}(x)$ at the two ends of the cell, we have

$$\Phi_i^{\mathrm{L}}\left(x_{i-(1/2)}\right) = {}^{0}\overline{\phi}_{i-(1/2)}^n \tag{35}$$

and

$$\Phi_i^{\mathrm{L}}\left(x_{i+(1/2)}\right) = {}^{0}\overline{\phi}_{i+(1/2)}^n. \tag{36}$$

A constraint for the conservation of cell-integrated average is imposed as

$$\frac{1}{\Delta x_i}\int_{x_{i-(1/2)}}^{x_{i+(1/2)}} \Phi_i^{\mathrm{L}}(x)\,\mathrm{d}x = {}^{x}\overline{\phi}_i^n. \tag{37}$$

Another constrained condition for the interpolation construction is imposed on the first-order derivative of $\Phi_i^{\mathrm{L}}(x)$, at the middle point of the cell

$$\frac{\mathrm{d}\Phi_i^{\mathrm{L}}(x)}{\mathrm{d}x} = d_i^n. \tag{38}$$

The slope of the interpolation function at the cell center d_i^n remains as a free parameter to be determined. This parameter provides us a way to modify the interpolation function for reducing numerical diffusion and suppressing numerical oscillation. Some practical candidates for computing it were given in [33].

In terms of ${}^{0}\overline{\phi}_{i-(1/2)}^n$, ${}^{0}\overline{\phi}_{i+(1/2)}^n$, d_i^n and ${}^{x}\overline{\phi}_i^n$, the polynomial (34) can be completely determined with (35)–(38), and the coefficients read

$$c_{1i}^{\mathrm{L}} = -\frac{6}{\Delta x_i}{}^{x}\overline{\phi}_i^n + \frac{6}{\Delta x_i}{}^{0}\overline{\phi}_{i+(1/2)}^n - 2d_i^n, \tag{39}$$

$$c_{2i}^{\mathrm{L}} = -\frac{6}{\Delta x_i^2}{}^{x}\overline{\phi}_i^n + \frac{3}{\Delta x_i^2}\left(3{}^{0}\overline{\phi}_{i+(1/2)}^n - {}^{0}\overline{\phi}_{i-(1/2)}^n\right) - \frac{6}{\Delta x_i}d_i^n, \tag{40}$$

$$c_{3i}^{\mathrm{L}} = \frac{4}{\Delta x_i^3}\left({}^{0}\overline{\phi}^{n}_{i+(1/2)} - {}^{0}\overline{\phi}^{n}_{i-(1/2)}\right) - \frac{4}{\Delta x_i^2} d_i^n. \tag{41}$$

Analogously, the right-bias Φ_i^{R} interpolation function in the following form

$$\Phi_i^{\mathrm{R}}(x) = {}^{0}\overline{\phi}^{n}_{i+(1/2)} + c_{1i}^{\mathrm{R}}\left(x - x_{i+(1/2)}\right) + c_{2i}^{\mathrm{R}}\left(x - x_{i+(1/2)}\right)^2 + c_{3i}^{\mathrm{R}}\left(x - x_{i+(1/2)}\right)^3 \quad \text{for } x \in \left[x_{i-(1/2)}, x_{i+(1/2)}\right], \tag{42}$$

can also be derived from the same constraint conditions.

Once the interpolation function is determined, the SIA ${}^{0}\overline{\phi}$ at time step $n+1$ is firstly updated by a semi-Lagrangian solution as

$${}^{0}\overline{\phi}^{*}_{i+(1/2)} = \begin{cases} \Phi_i^{\mathrm{R}}(x_{i+(1/2)} + \alpha) & \text{if } \alpha < 0, \\ \Phi_{i+1}^{\mathrm{L}}(x_{i+(1/2)} + \alpha) & \text{if } \alpha > 0. \end{cases} \tag{43}$$

and corrected according to the divergence of the velocity field

$${}^{0}\overline{\phi}^{n+1}_{i+(1/2)} = {}^{0}\overline{\phi}^{*}_{i+(1/2)} - \int_{\tau}\left(\phi\frac{\partial u}{\partial x}\right)\mathrm{d}\tau', \tag{44}$$

where τ is the trajectory through which the semi-Lagrangian particle travels during Δt. We use the following approximation in this study

$$\int_{\tau}\left(\phi\frac{\partial u}{\partial x}\right)\mathrm{d}\tau' = \begin{cases} 0.5\,{}^{0}\overline{\phi}^{*}_{i+(1/2)}\left({}^{0}\overline{u}^{*}_{i+(1/2)} - {}^{0}\overline{u}^{*}_{i-(1/2)} + {}^{0}\overline{u}^{n}_{i+(1/2)} - {}^{0}\overline{u}^{n}_{i-(1/2)}\right)\Delta t/\Delta x_i & \text{if } \alpha < 0, \\ 0.5\,{}^{0}\overline{\phi}^{*}_{i+(1/2)}\left({}^{0}\overline{u}^{*}_{i+(3/2)} - {}^{0}\overline{u}^{*}_{i+(1/2)} + {}^{0}\overline{u}^{n}_{i+(3/2)} - {}^{0}\overline{u}^{n}_{i+(1/2)}\right)\Delta t/\Delta x_{i+1} & \text{if } \alpha > 0, \end{cases} \tag{45}$$

where u^* is the provisional value of the velocity right after the semi-Lagrangian solution in fluid computation. The displacement is estimated by a Taylor approximation up to third order [17] as

$$\alpha = -u_{i+(1/2)}\Delta t + \frac{1}{2}u_{i+\frac{1}{2}}(\Delta t)^2\left(\frac{\partial u}{\partial z}\right)_{i+(1/2)} - \frac{1}{6}u_{i+(1/2)}(\Delta t)^3\left[\left(\frac{\partial u}{\partial z}\right)^2_{i+\frac{1}{2}} + u_{i+(1/2)}\left(\frac{\partial^2 u}{\partial z^2}\right)_{i+(1/2)}\right], \tag{46}$$

where $(\partial u/\partial z)_{i+(1/2)}$ and $(\partial^2 u/\partial z^2)_{i+(1/2)}$ are computed by central differencing.

The VIA ${}^{x}\overline{\phi}$ is advanced by a flux form from the conservative relation

$${}^{x}\overline{\phi}^{n+1}_{i} = {}^{x}\overline{\phi}^{n}_{i} - \left(g_{i+(1/2)} - g_{i-(1/2)}\right)/\Delta x_i, \tag{47}$$

where $g_{i+(1/2)}$ represents the flux across boundary $x = x_{i+(1/2)}$ during $t^{n+1} - t^n$ and is computed as

$$g_{i+(1/2)} = \int_{x_{i+(1/2)}+\alpha}^{x_{i+(1/2)}} \Phi_i^{\mathrm{R}}(x)\,\mathrm{d}x \quad \text{for } \alpha < 0, \tag{48}$$

$$g_{i+(1/2)} = -\int_{x_{i+(1/2)}}^{x_{i+(1/2)}+\alpha} \Phi_{i+1}^{\mathrm{L}}(x)\,\mathrm{d}x \quad \text{for } \alpha > 0. \tag{49}$$

As shown in [33], the reconstructed profile can be easily modified in the CIP-CSL3 scheme by the slope parameter d_i^n. Numerical oscillation can be effectively suppressed if we approximate d_i^n by using the following formulation [25]

$$\hat{d}_i = \text{minmod}\left(\frac{S_{i+(1/2)} + S_{i-(1/2)}}{2}, 2S_{i+(1/2)}, 2S_{i-(1/2)}\right), \tag{50}$$

with $S_{i+(1/2)} = 2(\phi_{i+1} - \phi_i)/(\Delta x_i + \Delta x_{i+1})$. As given in [33], the 'point-value' of the interpolation function at cell center can be computed as

$$\phi_i = \tfrac{3}{2}\overline{{}^{x}\phi}_i^n - \tfrac{1}{4}\left(\overline{{}^{0}\phi}_{i+(1/2)}^n + \overline{{}^{0}\phi}_{i-(1/2)}^n\right). \tag{51}$$

A simple modification to artificially control the numerical diffusion and compression can be made by re-writing the slope parameter as

$$d_i^n = \beta_i \hat{d}_i. \tag{52}$$

The parameter β_i functions as a modification to the slope. It is obvious that any β_i larger than one will enforce the local sharpness of each piece-wisely constructed profile, while a β_i less than one will produce extra numerical diffusion to the solution. Fig. 2 shows the numerical results with different β_i. Without producing numerical oscillations, the numerical diffusion and the artificial compression can be effectively controlled by simply changing the values of β_i. Throughout the numerical tests presented in this paper the following solution dependent formula for β_i is used.

$$\beta_i = \begin{cases} 0.0125 & \text{if } \overline{{}^{0}u}_{i-(1/2)}^n - \overline{{}^{0}u}_{i+(1/2)}^n > 0.01\Delta x_i, \\ 1.2 & \text{otherwise.} \end{cases} \tag{53}$$

It is clear from (53) that a 'flatter' interpolation function is used in the region where velocity converges, which indicates the existence of a shock. As given in (53), the parameter β is a dimensionless positive and depending on the local gradient of the velocity field. We should note that the determination of β is somewhat arbitrary and might be problem dependent. The values specified in (53) has been determined from numerical experiments in the present study. We find that (53) works well with all numerical test reported in this paper.

2.4. Remarks on the conservation

In the present formulation, the pressure is an auxiliary variable needed for computing the non-advection fluxes of momentum and total energy. The pressure itself is not a conservative quantity in physics, and is solved in the non-advection part through a way similar to that in the projection method for incompressible flow. The original conservative variables, such as density, momentum and total energy are the dependent variables solved in the present method.

The discretization algorithm can be designed so that the volume integrated averages (VIAs) of the conservative variables in the original continuum system, i.e., density, momentum and total energy, are numerically conserved. In regard to the conservation of the whole discretization procedure, we have the following facts.

Proposition 1. *The volume integrated averages (VIAs) of density, momentum and total energy are exactly conserved in the advection computation if the CIP_CSL3 scheme is used.*

Proof. It is trivial to understand this by just observing the fact that in CIP_CSL3 scheme the volume integrated average (VIA) of the advected quantity is computed in a flux form (47). □

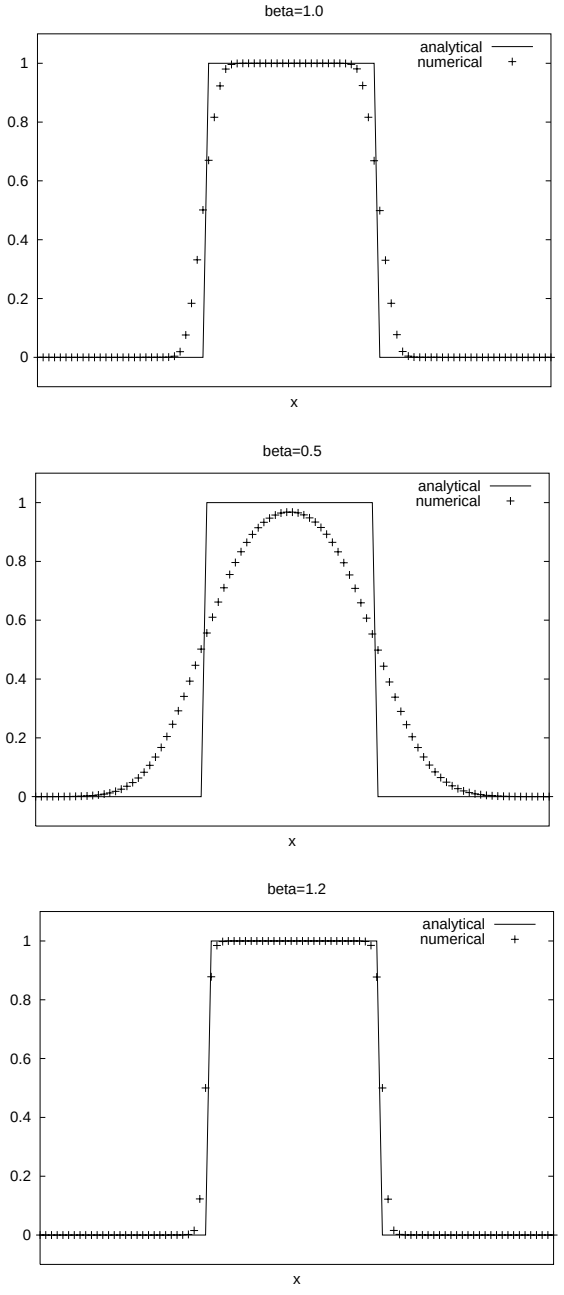

Fig. 2. Transport of a square wave computed by CSL3 with β_i in (52) being 1.0 (top), 0.5 (middle) and 1.2 (bottom). Plotted are the numerical results after 1000 steps with CFL = 0.26.

Proposition 2. *For a grid with uniform spacing, the TEC formula* (30) *and* (32)*, with the SIAs of momentum and total energy updated by* (29) *and* (31)*, conserve the VIAs of momentum and total energy in the non-advection part.*

Proof. Assuming the grid is equally spaced with $\Delta x_i = \Delta x$, we write the (29) and (31) as

$$\overline{{}^{0}m}_{i+(1/2)}^{n+1} = \overline{{}^{0}m}_{i+(1/2)}^{\diamondsuit} - \Delta t \frac{\overline{{}^{x}p}_{i+1}^{n+1} - \overline{{}^{x}p}_{i}^{n+1}}{\Delta x} \tag{54}$$

and

$$\overline{{}^{0}E}_{i+(1/2)}^{n+1} = \overline{{}^{0}E}_{i+(1/2)}^{\diamondsuit} - \Delta t \frac{\overline{{}^{x}u}_{i+1}^{n+1}\overline{{}^{x}p}_{i+1}^{n+1} - \overline{{}^{x}u}_{i}^{n+1}\overline{{}^{x}p}_{i}^{n+1}}{\Delta x}. \tag{55}$$

Substituting (54) and (55) into (30) and (32), respectively, we obtain

$$\overline{{}^{x}m}_{i}^{n+1} = \overline{{}^{x}m}_{i}^{\diamondsuit} + \tfrac{1}{2}(\overline{{}^{0}m}_{i+(1/2)}^{n+1} - \overline{{}^{0}m}_{i+(1/2)}^{\diamondsuit} + \overline{{}^{0}m}_{i-(1/2)}^{n+1} - \overline{{}^{0}m}_{i-(1/2)}^{\diamondsuit}) = \overline{{}^{x}m}_{i}^{\diamondsuit} - \Delta t \frac{p_{i+(1/2)}^{n+1} - p_{i-(1/2)}^{n+1}}{\Delta x} \tag{56}$$

and

$$\overline{{}^{x}E}_{i}^{n+1} = \overline{{}^{x}E}_{i}^{\diamondsuit} + \tfrac{1}{2}(\overline{{}^{0}E}_{i+(1/2)}^{n+1} - \overline{{}^{0}E}_{i+(1/2)}^{\diamondsuit} + \overline{{}^{0}E}_{i-(1/2)}^{n+1} - \overline{{}^{0}E}_{i-(1/2)}^{\diamondsuit}) = \overline{{}^{x}E}_{i}^{\diamondsuit} - \Delta t \frac{(up)_{i+(1/2)}^{n+1} - (up)_{i-(1/2)}^{n+1}}{\Delta x}, \tag{57}$$

where $p_{i+(1/2)}^{n+1} = (\overline{{}^{x}p}_{i+1}^{n+1} + \overline{{}^{x}p}_{i}^{n+1})/2$ and $(up)_{i+(1/2)}^{n+1} = (\overline{{}^{x}u}_{i+1}^{n+1}\overline{{}^{x}p}_{i+1}^{n+1} + \overline{{}^{x}u}_{i}^{n+1}\overline{{}^{x}p}_{i}^{n+1})/2$.

The TEC formula (56) and (57) are of flux form, and equivalent to the collocated central scheme in terms of VIA variables. □

Proposition 3. *For a grid with non-uniform spacing, the conservation of the VIAs of momentum and total energy can be assured if the following TEC formula are used,*

$$\overline{{}^{x}m}_{i}^{n+1} = \overline{{}^{x}m}_{i}^{\diamondsuit} + \frac{1}{4\Delta x_i}\left[(\Delta x_i + \Delta x_{i+1})\left(\overline{{}^{0}m}_{i+(1/2)}^{n+1} - \overline{{}^{0}m}_{i+(1/2)}^{\diamondsuit}\right) + (\Delta x_i + \Delta x_{i-1})\left(\overline{{}^{0}m}_{i-(1/2)}^{n+1} - \overline{{}^{0}m}_{i-(1/2)}^{\diamondsuit}\right)\right] \tag{58}$$

and

$$\overline{{}^{x}E}_{i}^{n+1} = \overline{{}^{x}E}_{i}^{\diamondsuit} + \frac{1}{4\Delta x_i}\left[(\Delta x_i + \Delta x_{i+1})\left(\overline{{}^{0}E}_{i+(1/2)}^{n+1} - \overline{{}^{0}E}_{i+(1/2)}^{\diamondsuit}\right) + (\Delta x_i + \Delta x_{i-1})\left(\overline{{}^{0}E}_{i-(1/2)}^{n+1} - \overline{{}^{0}E}_{i-(1/2)}^{\diamondsuit}\right)\right]. \tag{59}$$

Proof. The following conservative formula of flux-form can be immediately obtained by combining (29) and (31) with (58) and (59), respectively,

$$\overline{{}^{x}m}_{i}^{n+1} = \overline{{}^{x}m}_{i}^{\diamondsuit} - \Delta t \frac{p_{i+(1/2)}^{n+1} - p_{i-(1/2)}^{n+1}}{\Delta x_i} \tag{60}$$

and

$$\overline{{}^{x}E}_{i}^{n+1} = \overline{{}^{x}E}_{i}^{\diamondsuit} - \Delta t \frac{(up)_{i+(1/2)}^{n+1} - (up)_{i-(1/2)}^{n+1}}{\Delta x_i}. \tag{61}$$

The conservation of the VIAs then follows. □

In a VSIAM3 formulation, the SIA quantities are not necessarily conserved, while the VIAs can be computed in an exactly conservative manner. The conservation of VSIAM3 will be tested with strong shocks containing extremely large jumps and high Mach flow in Section 3.

Before end this subsection, it should be mentioned that conservative formulation can also be constructed under a framework where the pressure is computed as a dependent variable [26].

2.5. Remarks on incompressible flow computation

Consider the incompressible flow to be the case when the sound speed C becomes infinity, we have

$$\frac{\partial^2 p^{n+1}}{\partial x^2} = \frac{1}{\Delta t}\left(- u^{\diamondsuit} \frac{\partial \rho^{n+1}}{\partial x} + \frac{\partial m^{\diamondsuit}}{\partial x} \right) \tag{62}$$

by dropping out the term including C from (10) . For an incompressible flow of uniform density in multi-dimensions, Eq. (62) is equivalent to

$$\nabla^2 p^{n+1} = \frac{1}{\Delta t}\rho \nabla \cdot \mathbf{V}^{\diamondsuit}. \tag{63}$$

It is the Poisson pressure equation in the projection method of Chorin [4], Kim and Moin [16] and many others. In our multi-integrated moment scheme, the SIAs of the velocity components in the normal directions which are defined on each surface segment of the control volume are employed to compute the divergence. The pressure in (63) is interpreted as the VIA quantity. In the incompressible case, the fractional step procedure described above resembles the projection method but has different discretizations due to the use of multi-integrated moments.

Being the thermodynamic quantity that directly drives the fluid motion, pressure is solved implicitly in the pressure based methodology which removes the singularity in the computation of incompressible flows and leads to a class of projection methods. The pressure in the complete incompressible case plays a numerical role to eliminate divergence in the velocity field rather than a state variable of thermodynamics as in the compressible flow. The pressure equation then becomes an elliptic form (63) from its original parabolic type (10).

Multi-dimensional model for low Mach number and for incompressible flow, which corresponding the case of $C \to \infty$, will be presented in a separate paper with numerical tests, where we have found that our numerical model also gave good results to the benchmark tests for the incompressible flow computations. We will only consider the compressible flows in the present paper.

3. Numerical tests

3.1. Comparisons with existing pressure-correction method

To compare the presented method with other pressure based formulations, we have computed the test problems in [26], where three tests of 1D compressible flow, namely Sod's problem, Lax's problem and non-stationary contact discontinuity, are used to evaluate the conservative and the non-conservative pressure-correction schemes of the authors. To make the numerical results directly comparable, our numerical experiments were carried out with the same conditions as those given in [26]. Fig. 3 are the results of the present scheme for the Sod's problem. Compared to Figs. 3 and 4 in [26], it is obvious that the VSIAM3 scheme produces much more accurate solutions than the cited schemes. The shock wave is well resolved with a correct displacement, and the entropy overshoot across the shock associated with the staggering of the velocity and the scalar quantities, as mentioned in [26], is not observed in present result. For the 1D shock tube problem of Lax, the same conclusions can be drawn by simply comparing Fig. 4 with Figs. 6, 7 and 8 in [26]. The non-stationary contact discontinuity was also computed with the results plotted in Fig. 5.

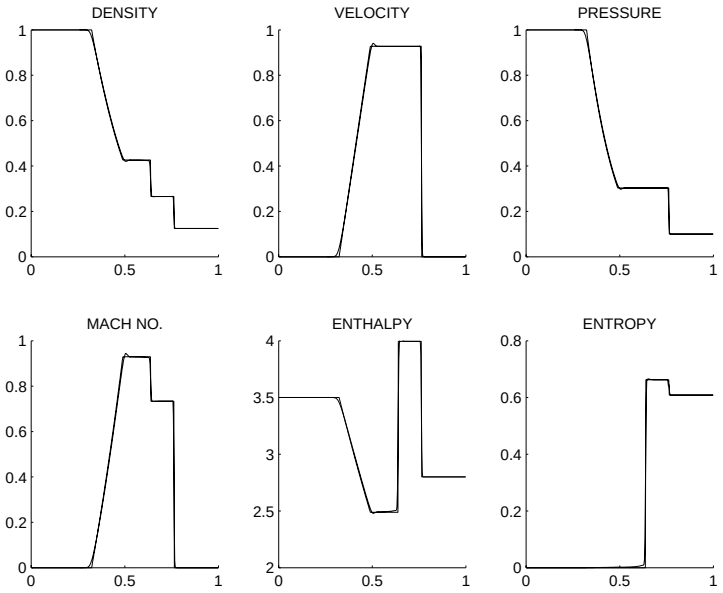

Fig. 3. Numerical results of the Sod's problem at $t = 0.15$. Computational conditions and the way of display are the same as in [26] for comparison with their Figs. 3–5.

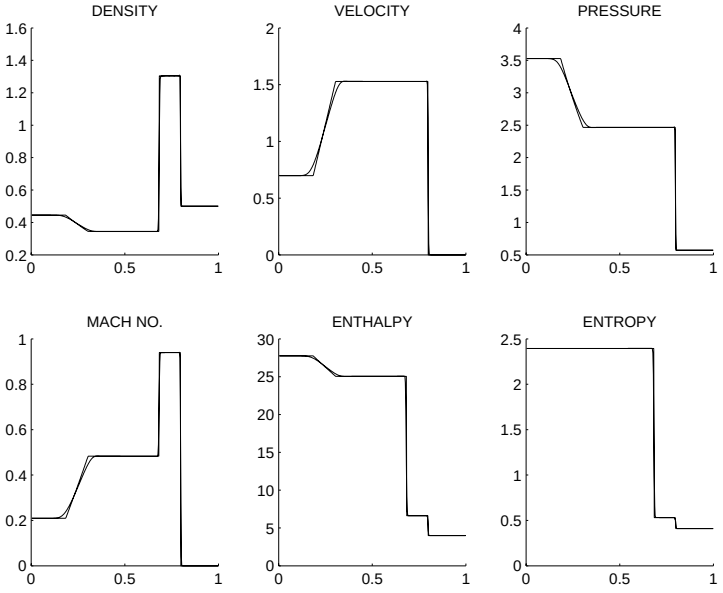

Fig. 4. Numerical results of the Lax's problem at $t = 0.12$. Computational conditions and the way of display are the same as in [26] for comparison with their Figs. 6–8.

Compared with the corresponding numerical results in [26], we find that the present scheme gives much crisper contact discontinuity. This configuration generates only a linear contact wave with a discontinuous jump in density, which moves at the constant advection velocity given in the initial condition. It is clear that

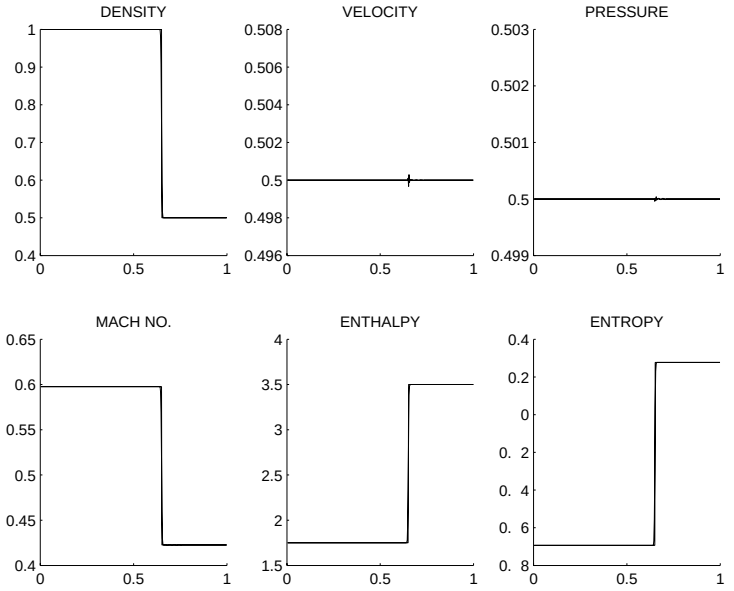

Fig. 5. Numerical results of the moving contact discontinuity at $t = 0.3$. Computational conditions and the way of display are the same as in [26] for comparison with their Figs. 9–11.

the only physical process that functions in this test is the advection. It seems that the fractional step solution procedure as used in the present method show a merit for handling this type of linear contact waves. The advection scheme, CIP_CSL3, gives a satisfactory solution. However, it should be also noted that VSIAM3 scheme produced some tiny oscillations in the velocity field, even which is much smaller than those occur the non-conservative pressure-correction method in [26].

Another issue we should mention is that the first-order upwind scheme was used in the numerical tests in [26], so the numerical results were very smearing there as expected. Thus, the numerical results of VSIAM3 look distinctly superior. So, it should be also interesting to compare VSIAM3 with other popular schemes that use high order reconstructions.

3.2. Comparisons with other high resolution methods

Next, we compare VSIAM3 with other high resolution schemes which use higher order interpolation reconstructions. We chose two representative high resolution shock capturing schemes, a TVD scheme and a WENO scheme. In the TVD scheme, the MUSCL reconstruction [25], the van Albada limiter [1] and a two-step time integration are incorporated to the flux difference scheme of Roe [20]. The WENO scheme is the third-order scheme of Jiang and Shu [13]. The Sod's 1D shock wave problem [21] was computed on a 400-point grid, and the numerical results are plotted in Fig. 6. The result of VSIAM3 looks competitive to the other two's, but gives a more smeared expansion front and a crisper contact discontinuity. The enlarged parts for shock and contact discontinuity are displayed in Figs. 7 and 8. All schemes accurately reproduced the shock with a correct position and a compact thickness. The VSIAM3 has a tiny overshoot right after the shock. Compared to the TVD scheme, the VSIAM3 and the WENO schemes give crisper contact discontinuities. It should be noted that the numerical diffusion to the contact discontinuity can be improved also in the TVD and WENO schemes by separately devised artificial compressions [9,40]. A more detailed comparison is conducted by examining the l_2 errors of the different schemes. As shown in Table 1, the

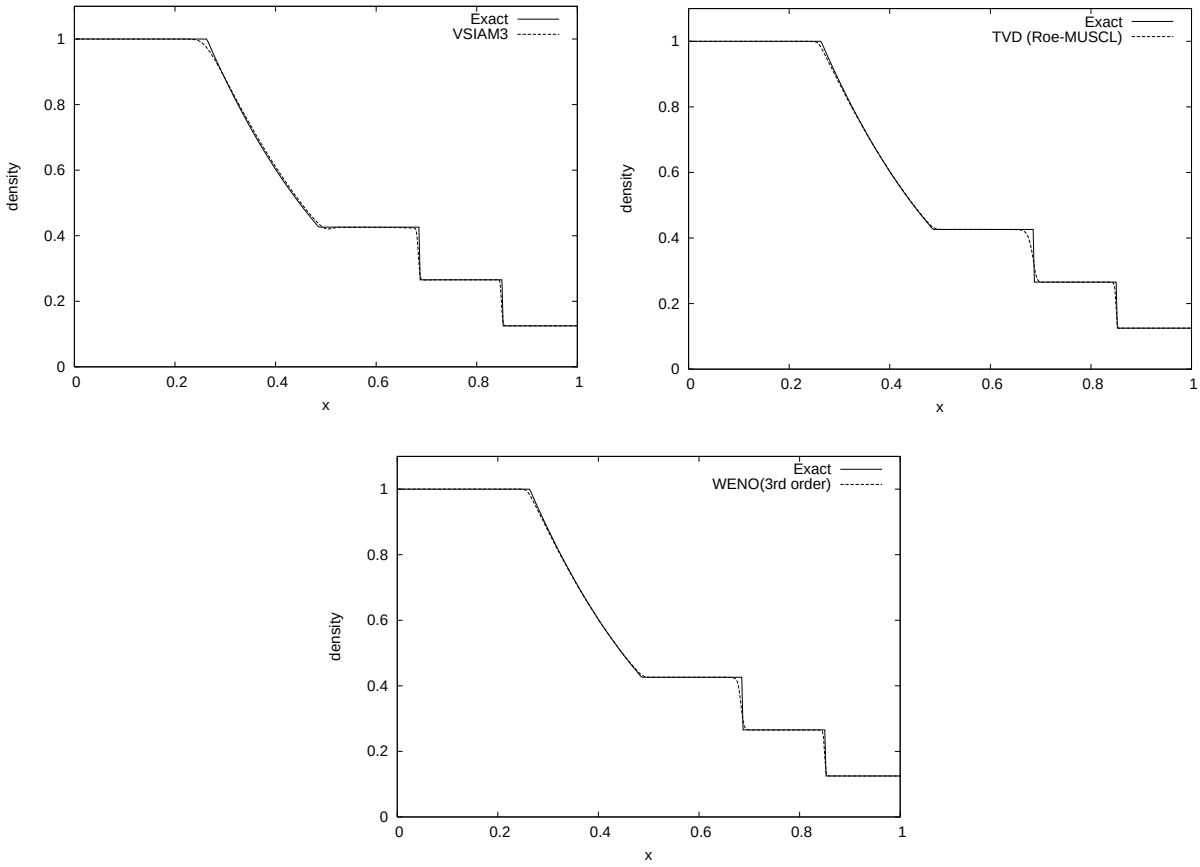

Fig. 6. Sod's problem computed by VSIAM3, Roe-MUSCL TVD and third-order WENO. Displayed are the results (density) at $t = 0.2$ with the CFL number being 0.15.

overall accuracy of the VSIAM3 lies between the Roe-MUSCL TVD scheme and the third-order WENO scheme. The convergence with respect to grid refinement can be obtained by comparing the errors on different grid resolutions. The VSIAM3 converges at a rate similar to the conventional high resolution schemes.

3.3. Supersonic shock with extremely large pressure and velocity jumps

An extremely strong shock tube problem is computed by VSIAM3 to examine the conservative nature and the robustness of the scheme. The initial condition is given on the 1D computational domain, $0 \leqslant x \leqslant 1$, as follows:

$$(\rho, u, p) = \begin{cases} (1, 0, 1.0 \times 10^{10}) & \text{for } x \leqslant 0.5, \\ (0.125, 0, 0.1) & \text{for } x > 0.5. \end{cases} \tag{64}$$

This initial condition creates a supersonic shock associated with very large jumps in velocity and pressure. It is a quite severe problem to test not only the stability and robustness, but also the conservation

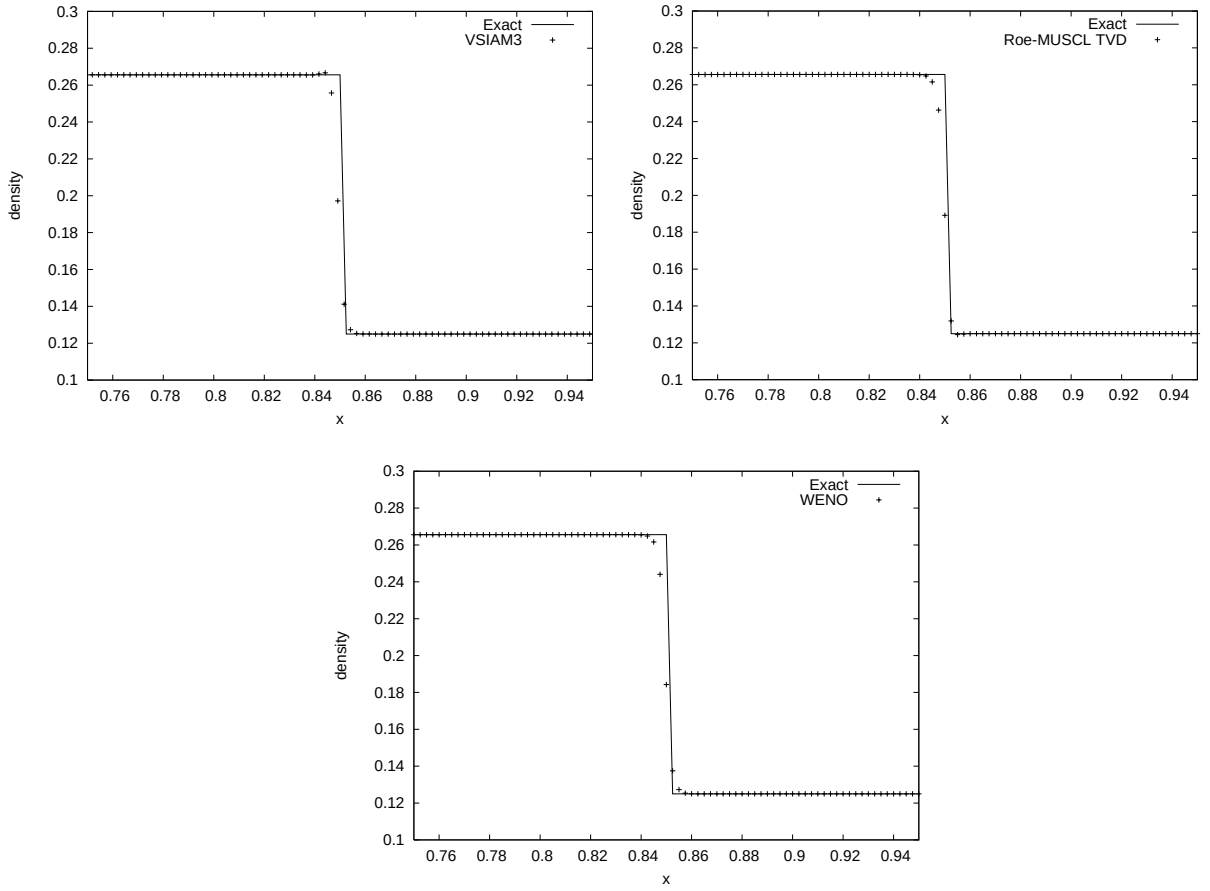

Fig. 7. Sod's problem computed by VSIAM3, Roe-MUSCL TVD and third-order WENO. Displayed are the results (density) at $t = 0.2$ with the CFL number being 0.15 (enlarged part of shock wave).

of numerical methods, because a non-conservative scheme tends to produce a wrong shock position especially in the case of strong shock.

A 400-point equally spaced grid is used. The time stepping interval is $\Delta t = 6.29 \times 10^{-9}$, and the CFL number based on the large velocity is about 0.3. The numerical results at $t = 2.5 \times 10^{-6}$ are shown in Fig. 9. The strong shock with the velocity jump of 1.18×10^5 and the pressure jump of 2.1×10^9 is accurately computed with a correct position. This reveals the conservative nature of VSIAM3 as discussed in the previous section.

The conservation is further examined by summing up the density and the total energy over the whole computational domain. The variations of the density and the total energy in respect to their initial values of the whole system are plotted in Figs. 10 and 11. As can be expected, the VIAs of both density and total energy are exactly conserved, while the SIA quantities experience some fluctuations with an order less than 0.1% in the relative errors.

3.4. High Mach shock tube

This test problem is to examine the performance of VSIAM3 on shocks of high Mach number. The initial condition is given on the 1D computational domain, $0 \leqslant x \leqslant 1$, as follows:

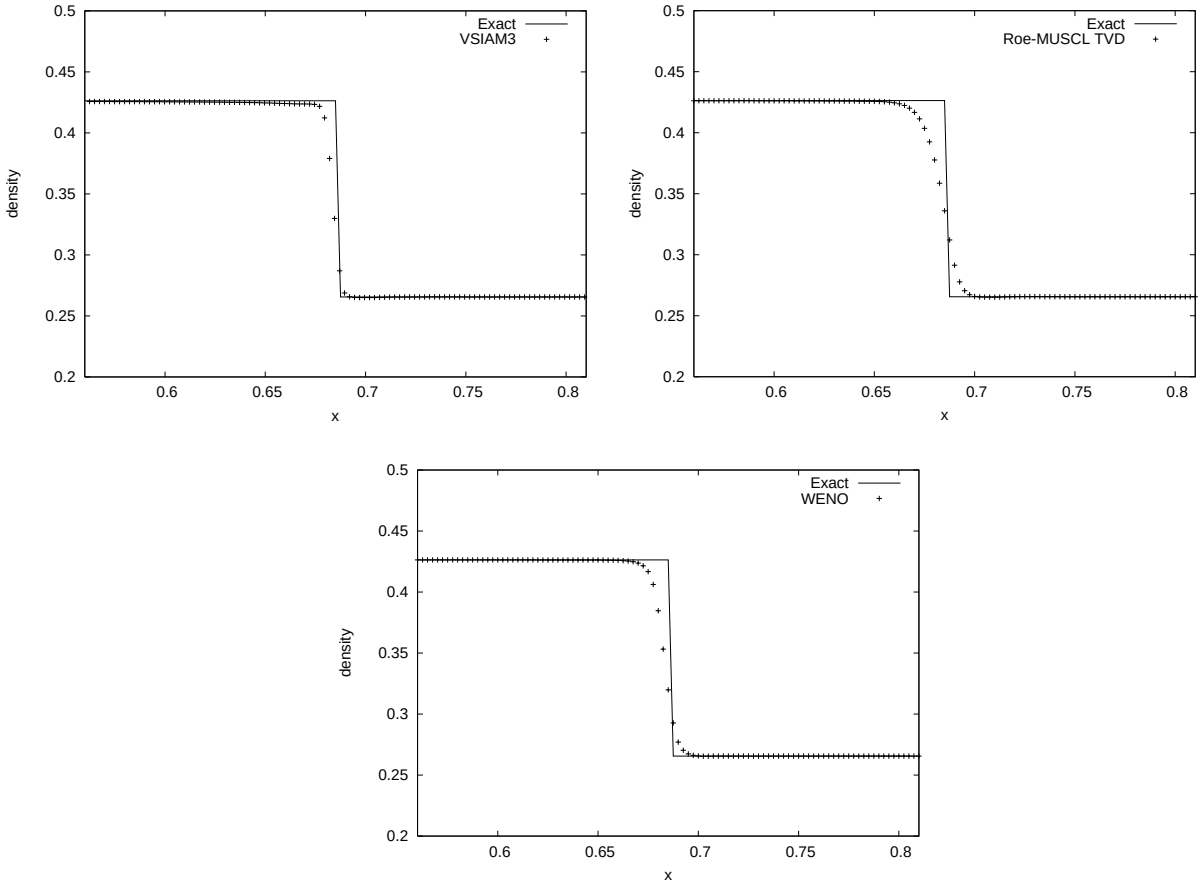

Fig. 8. Sod's problem computed by VSIAM3, Roe-MUSCL TVD and third-order WENO. Displayed are the results (density) at $t = 0.2$ with the CFL number being 0.15 (enlarged part of contact discontinuity).

Table 1
Grid refinement tests of Sod's problem

N	100	200	400
VSIAM3	2.07×10^{-3}	7.38×10^{-4}	3.64×10^{-4}
Roe-MUSCL TVD	1.49×10^{-3}	7.69×10^{-4}	3.97×10^{-4}
WENO (third order)	1.47×10^{-3}	6.85×10^{-4}	3.37×10^{-4}

Displayed are the errors defined by $E_{l_2} = \frac{1}{N}\sqrt{\sum_{i=1}^{N}(\rho_i^n - \rho_i^{\text{exact}})^2}$ with ρ being the density and N the number of grid cells.

$$(\rho, u, p) = \begin{cases} (10, 2000, 500) & \text{for } x \leqslant 0.5, \\ (20, 0, 500) & \text{for } x > 0.5. \end{cases} \tag{65}$$

Two shocks separated by a contact discontinuity are driven by a supersonic flow of Mach 239. A 400-point equally spaced grid is used. The time stepping interval is $\Delta t = 5.0 \times 10^{-7}$, and the maximum CFL number is 0.4. The numerical results at $t = 1.75 \times 10^{-4}$ are shown in Fig. 12. Two shocks are well reproduced with accurate position, while the contact discontinuity, which develops from the initial uniform

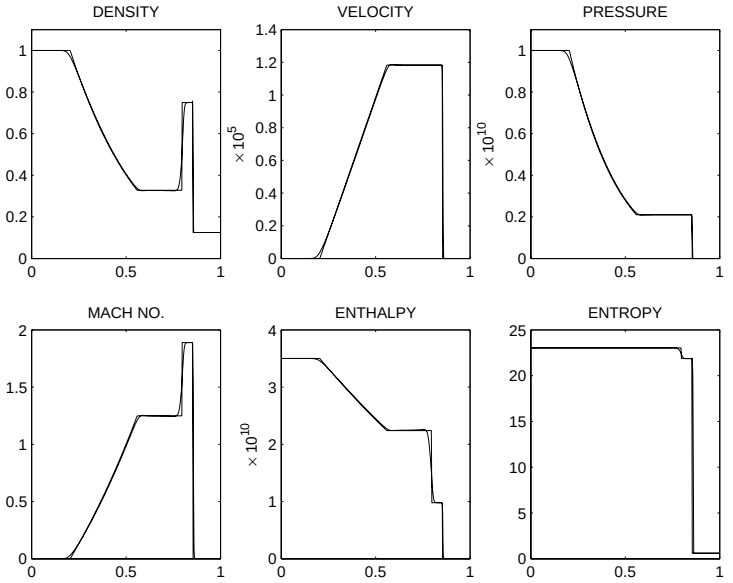

Fig. 9. Numerical results of strong shock wave at $t = 2.5 \times 10^{-6}$. The initial condition is given by (64). The plots of velocity, pressure and enthalpy are scaled by 10^5, 10^{10} and 10^{10}, respectively.

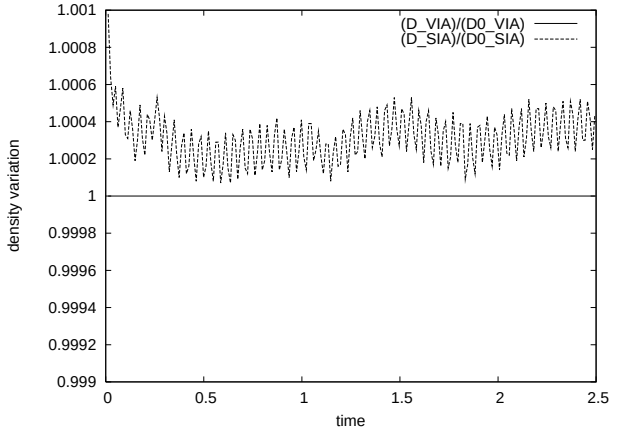

Fig. 10. The variation in the density integrated over the whole computational domain. Displayed are the ratio of the computed density at different instants against the initial density. The related quantities are defined as $\mathrm{D0\_SIA} = \sum_{i=1}^{i=N} [{}^{0}\overline{\rho(0)}_{i+(1/2)}]$, $\mathrm{D\_SIA} = \sum_{i=1}^{i=N} [{}^{0}\overline{\rho(t)}_{i+(1/2)}]$, $\mathrm{D0\_VIA} = \sum_{i=1}^{i=N} [{}^{x}\overline{\rho(0)}_{i}]$ and $\mathrm{D\_VIA} = \sum_{i=1}^{i=N} [{}^{x}\overline{\rho(t)}_{i}]$, where N is the grid number. The time is scaled by 10^{-6}.

density field rather than pre-exists, is much smeared than in the case of weak shock. Again, the conservation of the VIA quantities makes VSIAM3 work well with strong shocks of high Mach number.

3.5. Other benchmark tests

In order to further evaluate the present numerical method, we computed some other numerical tests suggested in [23] and other literature. The numerical method shows a satisfactory robustness for even severe cases for a wide range of the Mach number.

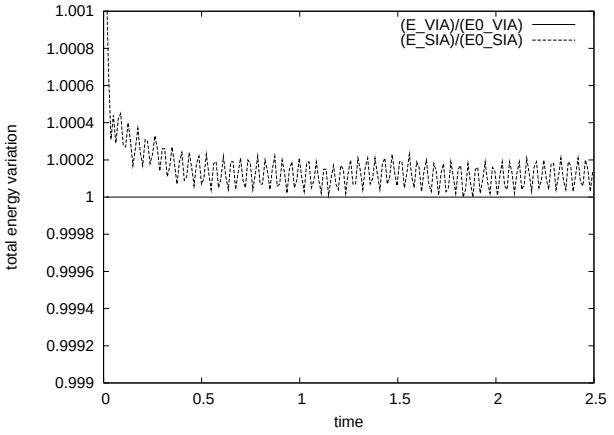

Fig. 11. The variation in the total energy integrated over the whole computational domain. Displayed are the ratio of the computed total energy at different instants against its initial value. The related quantities are defined as E0_SIA $= \sum_{i=1}^{i=N} [\overline{{}^{0}E(0)}_{i+(1/2)}]$, E_SIA $= \sum_{i=1}^{i=N} [\overline{{}^{0}E(t)}_{i+(1/2)}]$, E0_VIA $= \sum_{i=1}^{i=N} [\overline{{}^{x}E(0)}_{i}]$ and E_VIA $= \sum_{i=1}^{i=N} [\overline{{}^{x}E(t)}_{i}]$, where N is the grid number. The time is scaled by 10^{-6}.

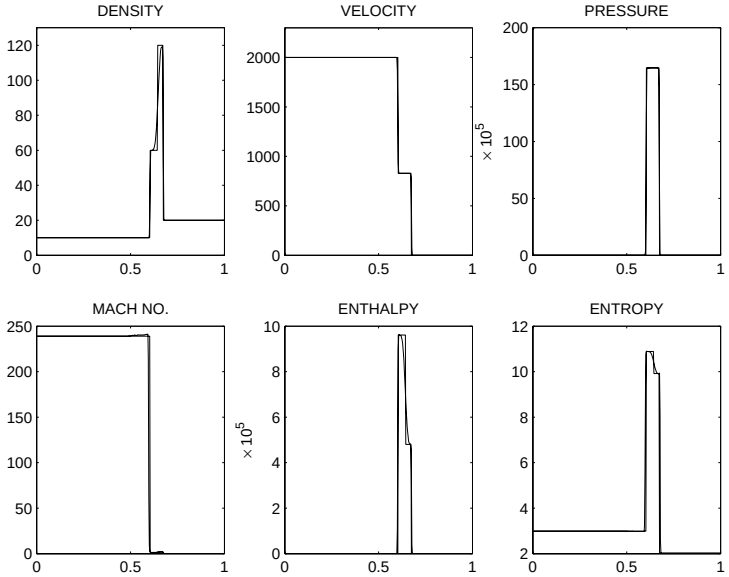

Fig. 12. Numerical results of a high Mach shock tube problem at $t = 1.75 \times 10^{-4}$. The initial condition is given by (65). The plots of pressure and enthalpy are scaled by 10^5.

In the following numerical tests except that of the interaction blast waves, the spatial domain of $0 \leqslant x \leqslant 1$ is partitioned equally into 100 mesh cells. The CFL number is set to 0.2 in respect to the maximum velocities in different cases, and the initial conditions are defined by the left-side state (ρ_l, u_l, p_l) and the right-side state (ρ_r, u_r, p_r) as

$$[\rho(x,0), u(x,0), p(x,0)] = \begin{cases} (\rho_l, u_l, p_l) & \text{for } x \leqslant 0.5, \\ (\rho_r, u_r, p_r) & \text{for } x > 0.5. \end{cases} \tag{66}$$

3.5.1. Two symmetric rarefaction waves

Two symmetric rarefaction waves and a zero speed contact wave are generated by the following initial conditions:

$$(\rho_l, u_l, p_l) = (1, -2, 0.4),$$
$$(\rho_r, u_r, p_r) = (1, 2, 0.4). \tag{67}$$

As mentioned in [23], because the region between the two non-linear rarefaction waves approaches to vacuum, this test is very useful to evaluate numerical methods for low density flows. The present method gives a stable numerical solution to this problem. Shown in Fig. 13, the density is well reproduced, while the pressure is slightly over estimated near the expansion center. The corresponding internal energy has then a pulse near the center of the low pressure region. It has been observed that this pulse in the internal energy is commonly produced by the algorithms based on the exact or Osher's Riemann solver, while the original Roe's Riemann solver failed on this test (see [23] for more discussions). Our numerical result is among those acceptable ones.

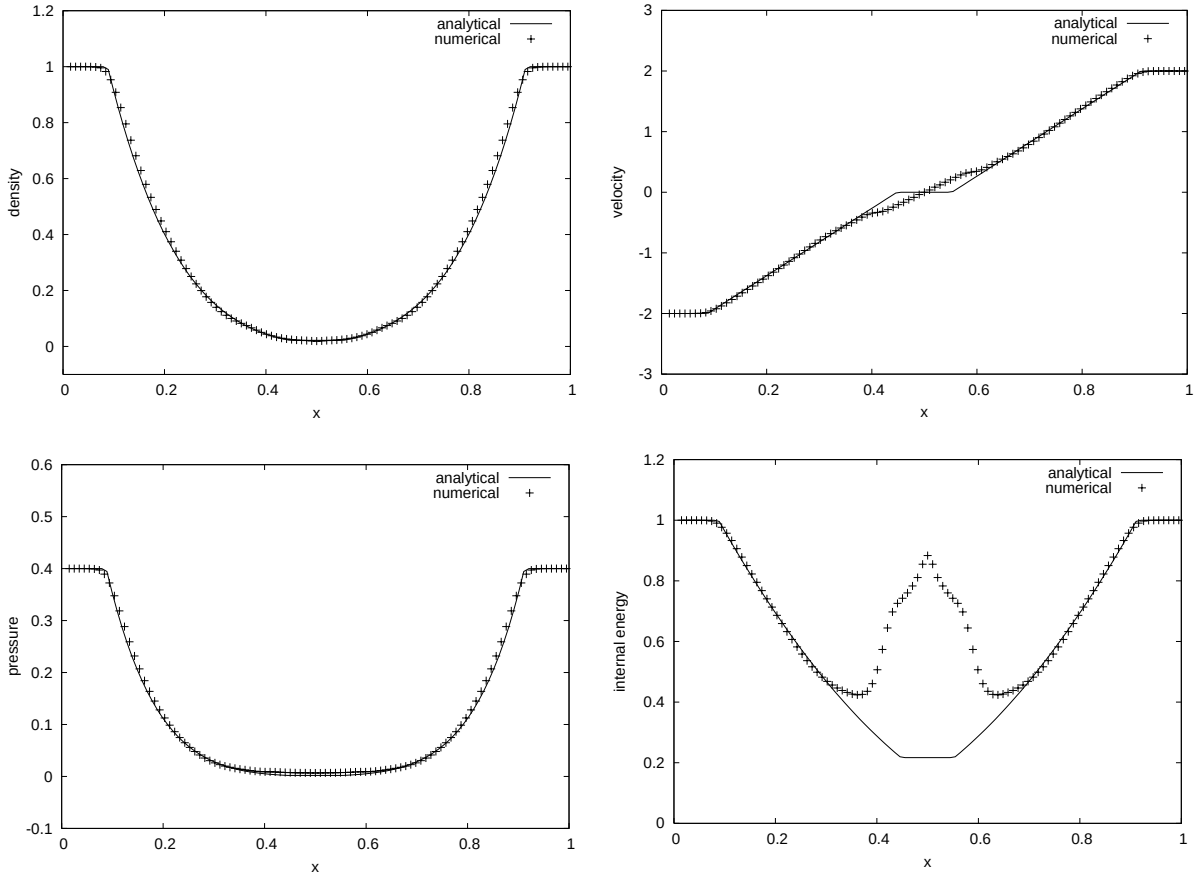

Fig. 13. Numerical results of symmetric expansion fans at $t = 0.15$. Displayed are density, velocity, pressure and internal energy.

3.5.2. Mach 3 shock

In this example, a Mach 3 shock is created by the following initial configuration [2]:

$$\begin{aligned}(\rho_l, u_l, p_l) &= (3.857, 0.92, 10.333),\\ (\rho_r, u_r, p_r) &= (1, 3.55, 1).\end{aligned} \tag{68}$$

The solution to this problem is characterized by a strong expansion fan containing sonic point. Shown in Fig. 14, a well-resolved expansion wave is obtained and the sonic glitch does not appear here. The right moving shock, which is a small jump in this case, is also identifiable in the numerical solution.

3.5.3. Stationary contact discontinuity

Similar to the moving contact discontinuity shown in the previous subsection, a stationary contact discontinuity is initially established by setting

$$\begin{aligned}(\rho_l, u_l, p_l) &= (1.4, 0, 1),\\ (\rho_r, u_r, p_r) &= (1, 0, 1).\end{aligned} \tag{69}$$

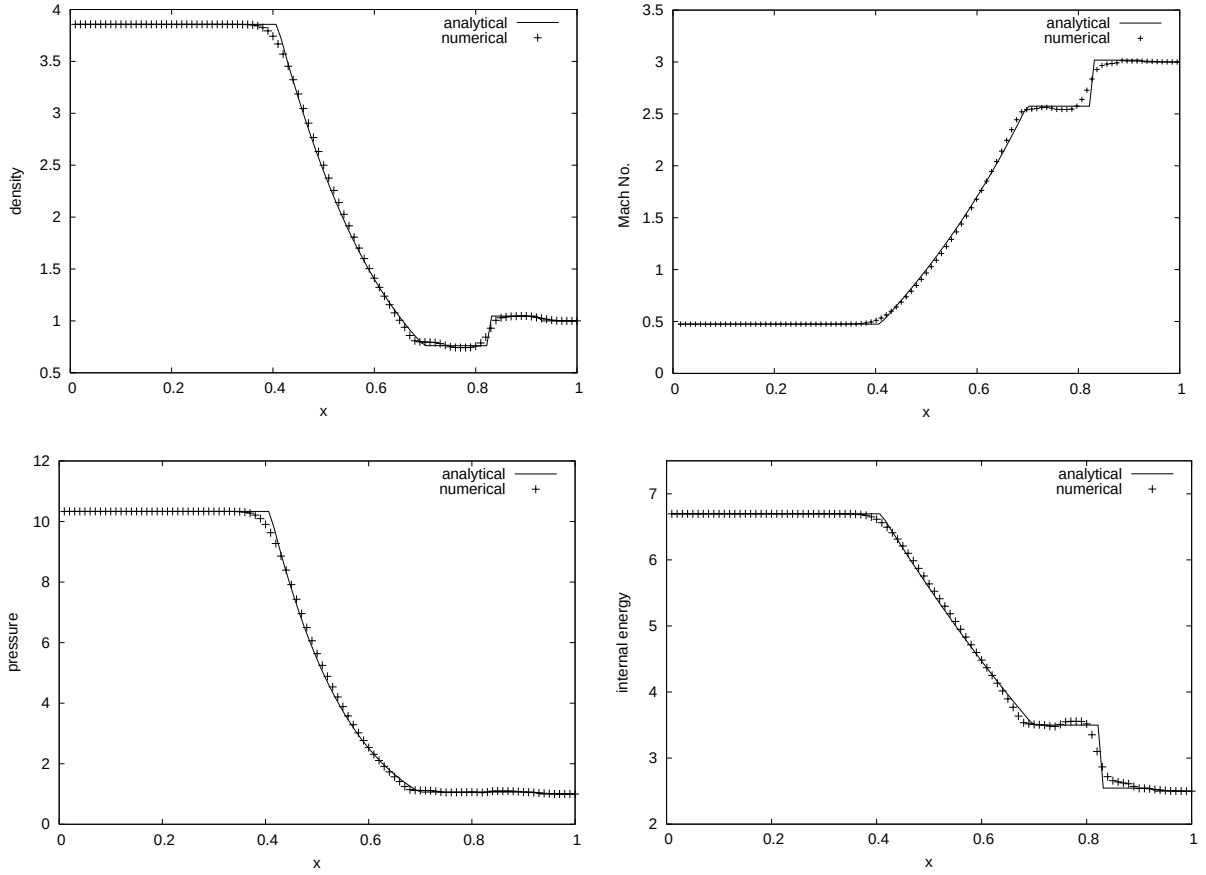

Fig. 14. Numerical results of the Mach 3 shock tube problem at $t = 0.09$. Displayed are density, Mach number, pressure and internal energy.

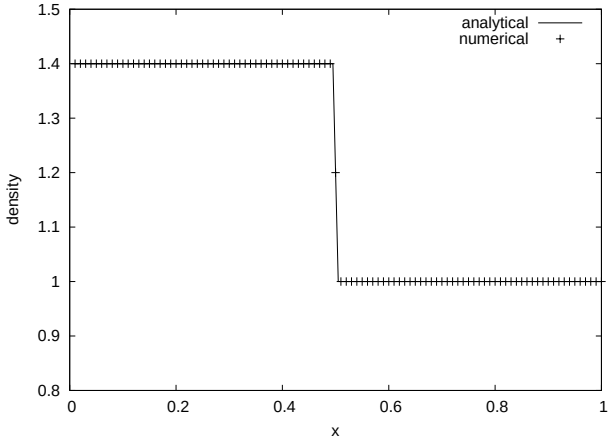

Fig. 15. The density profile of the stationary contact discontinuity at $t = 2$.

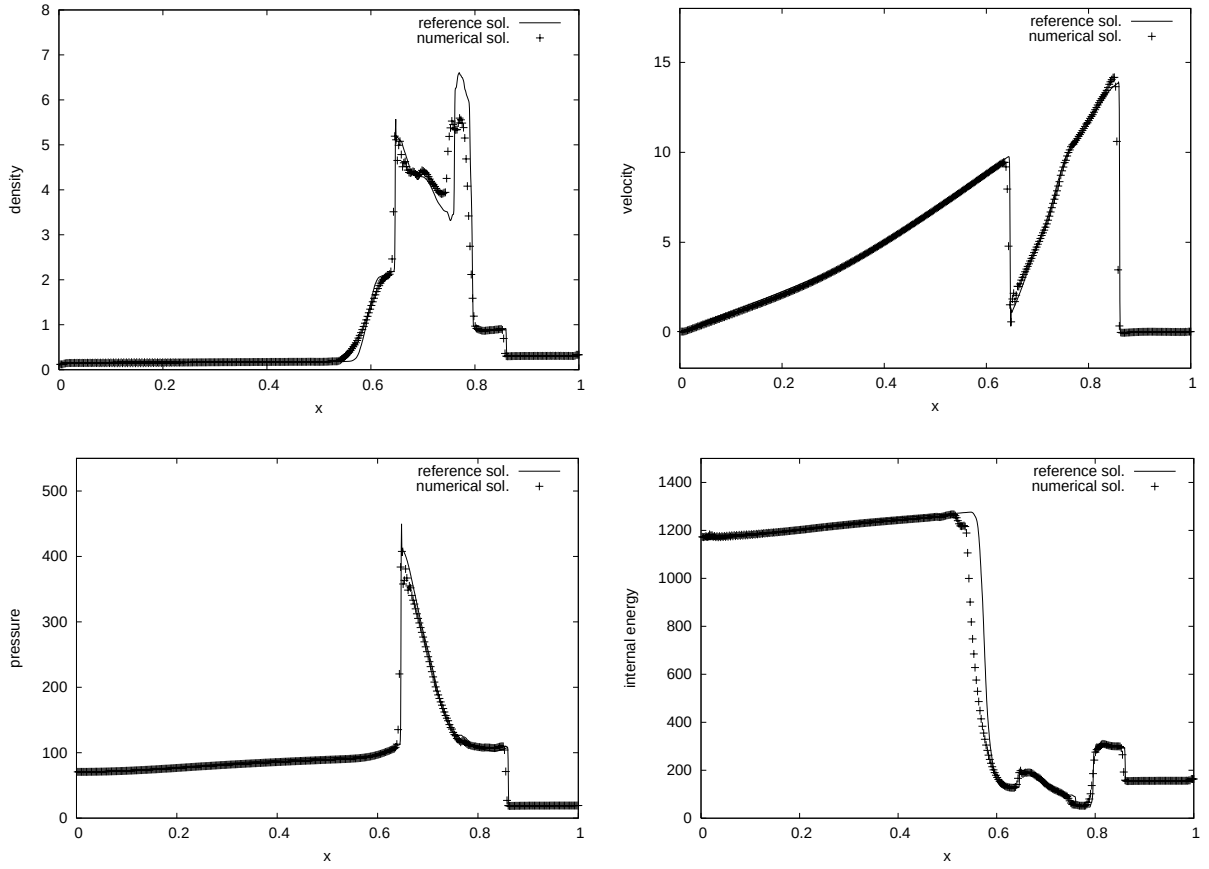

Fig. 16. Numerical results of two interacting blast waves at $t = 0.38$. Displayed are density, velocity, pressure and internal energy.

As can be expected, there should be not any motion. The solution should stay as its initial state. Shown in Fig. 15, the initial jump in density remains as its initial condition. Other physical quantities remain constant (not shown here).

3.5.4. Two interaction blast waves

The last test problem is the so called *two interaction blast waves* suggested in [30]. As discussed in [30], this problem involves multiple interactions among strong shocks, rarefaction waves and contact discontinuities, and is extremely difficult to solve on a uniform Eulerian grid. The computational domain is $0 \leqslant x \leqslant 1$, and the initial conditions are defined as

$$[\rho(x,0), u(x,0), p(x,0)] = \begin{cases} (1,0,1000) & \text{for } x < 0.1, \\ (1,0,0.01) & \text{for } 0.1 < x < 0.9, \\ (1,0,100) & \text{for } 0.9 < x < 1. \end{cases} \tag{70}$$

Two reflective walls are imposed at $x = 0$ and $x = 1$. We first computed the reference solution by using 1600 grid points. Comparing the numerical results shown in Fig. 16 with those in [30] and in other literature, we got a overall accurate reference solution where the displacements of the waves are correctly reproduced. The shocks are resolved sharply. We also observed small spurious oscillations right behind the left moving shock.

The numerical results with 400 grid points are also plotted in Fig. 16 against the reference solutions. We find that even with much fewer grid points the present scheme can still give acceptable numerical solutions with the correct positions of all waves. The major difference in the numerical solutions between 1600 stencils and 400 stencils is that the rarefaction wave on the left part of the solution is more smeared in the 400-cell computation.

4. Conclusions

We have presented a formulation for both the compressible and incompressible flows based on both the VIA and the SIA of the physical variables. A fractional step solution procedure is adopted with a pressure projection that includes the compressibility of the flow. The VIAs of density, momentum and total energy are solved in conservative form, which proves to be important to guarantee the correct displacements of the non-linear waves.

Using both VIA and SIAs of the physical variable enables us to make high order reconstruction with less mesh stencils. Since the VIA is positioned inside the control volume and the SIAs are on the surface segments, it is quite convenient to collocate the pressure or other thermodynamic variables with the VIAs of the velocity components. The pressure field, as we can see from the numerical solutions, are well coupled with the velocity field even without staggering the variables like those usually adopted in the conventional projection methods for incompressible flows. Moreover, we do not need the averaging of the velocity variables onto the staggered grid point for advection computation which is required in the conventional staggered grid for incompressible flows. However, we should note that since the SIAs are defined on the surface of a control volume, which are "staggered" in respect to the VIAs, difficulties may arise when applied to non-Cartesian grids. Nevertheless, the multi-dimensional formulation in a Cartesian grid comes straightforward. This will be discussed in a separate paper.

The advection scheme, CIP_CSL3, not only gives accurate solutions to the advection computations, but also provides us a simple device to control the numerical diffusion and artificial compression, thus improves significantly the numerical solutions. The multi-integrated moment formulation presented in this paper also

applies to other variants of the CIP_CSL schemes [34,37], and the VSIAM3 can be interpreted as a version of finite volume scheme of CIP method (FVM-CIP).

We have tested the presented scheme by computing various 1D benchmark problems for compressible flows. The numerical results show the robustness and the accuracy of the present method for a wide spectrum of test problems. Thus, we can expect the present method to be practical in many applications. As mentioned before, switching the present algorithm to the incompressible case is straightforward. The multi-dimensional formulation and the computations with weak compressibility will be reported in a separate paper.

Acknowledgements

The author gratefully acknowledges the helpful discussions with Prof. T. Yabe. He also thanks the three anonymous reviewers whose constructive comments leaded to a large improvement of the paper.

References

[1] G.D. van Albada, B. van Leer, W.W. Robert, A comparative study of computational methods in cosmic gas dynamics, Astron. Astrophys. 108 (1982) 76.
[2] M. Arora, P. Roe, A well-behaved TVD limiter for high resolution calculations of unsteady flow, J. Comput. Phys. 132 (1997) 3.
[3] H. Bijl, P. Wesseling, A unified method for computing incompressible and compressible flows in boundary-fitted coordinates, J. Comput. Phys. 141 (1998) 153.
[4] A. Chorin, Numerical solution of the Navier–Stokes equations, Math. Comput. 22 (1968) 745.
[5] H. Guillard, C. Viozat, On the behavior of upwind schemes in the low Mach number limit, Comput. Fluids 28 (1999) 63.
[6] F. Harlow, E. Welch, Numerical calculation of time-dependent viscous incompressible flow of fluid with a free surface, Phys. Fluids 8 (1965) 2182.
[7] F. Harlow, A. Amsden, Numerical calculation of almost incompressible flows, J. Comput. Phys. 3 (1968) 80.
[8] F. Harlow, A. Amsden, A numerical fluid dynamics calculation method for all flow speeds, J. Comput. Phys. 8 (1971) 197.
[9] A. Harten, The artificial compression method for computation of shocks and contact discontinuities. I. Single conservation laws, Commun. Pure Appl. Math. 30 (1977) 611.
[10] C.W. Hirt, Heuristic stability theory for finite-difference equations, J. Comput. Phys. 2 (1968) 339.
[11] R. Issa, Solution of the implicitly discretized fluid flow equations by operator-splitting, J. Comput. Phys. 62 (1986) 40.
[12] R. Issa, D. Gosman, A. Watkins, The computation of compressible and incompressible flows by a non-iterative implicit scheme, J. Comput. Phys. 62 (1986) 66.
[13] G.S. Jiang, C.W. Shu, Efficient implementation of weighted ENO schemes, J. Comput. Phys. 126 (1996) 202.
[14] C. Karki, S. Patankar, Pressure based calculation procedure for viscous flows at all speed in arbitrary configurations, AIAA J. 27 (1989) 1167.
[15] B. Koren, B. van Leer, Analysis of preconditioning and multigrid for Euler flows with low-subsonic regions, Adv. Comput. Methods 4 (1995) 127–144.
[16] J. Kim, P. Moin, Application of a fractional step method to incompressible Navier–Stokes equations, J. Comput. Phys. 59 (1985) 308.
[17] J. McGregor, Economical determination of departure points for semi-Lagrangian models, Mon. Wea. Rev. 121 (1993) 221.
[18] J. McGuirk, J. Page, Shock capturing using a pressure correction method, AIAA J. 28 (1990) 1751.
[19] Y. Ogata, T. Yabe, Shock capturing with improved numerical viscosity in primitive Euler representation, Comput. Phys. Commun. 119 (1999) 179.
[20] P.L. Roe, Approximate Riemann solvers, parameter vectors, and difference schemes, J. Comput. Phys. 43 (1981) 357.
[21] G. Sod, A survey of several finite difference methods for systems of non-linear conservation laws, J. Comput. Phys. 27 (1978) 1.
[22] W. Shyy, E. Braaten, Adaptive grid computation for inviscid compressible flows using a pressure correction method, AIAA paper 88-3566, 1988.
[23] E. Toro, Riemann Solvers and Numerical Methods for Fluid Dynamics, Springer, Berlin, 1997.
[24] E. Turkel, Review of preconditioning techniques for fluid dynamics, Appl. Numer. Math. 21 (1993) 257.
[25] B. van Leer, Toward the ultimate conservative difference scheme. Part V: a second order sequel to Godunov's method, J. Comput. Phys. 32 (1979) 101.

[26] D,R. van der Heul, C. Vuik, P. Wesseling, A conservative pressure-correction method for flow at all speeds, Comput. Fluids 32 (2003) 1113.
[27] M. Weiss, A. Smith, Preconditioning applied to variable and constant density flows, AIAA J. 22 (1995) 745.
[28] P. Wesseling, Principles of Computational Fluid Dynamics, Springer, Berlin, 2000.
[29] M.L. Wilkins, Use of artificial viscosity in multi-dimensional fluid dynamic calculations, J. Comput. Phys. 36 (1980) 281.
[30] P. Woodward, P. Colella, The numerical simulation of two-dimensional fluid flow with strong shocks, J. Comput. Phys. 54 (1984) 115.
[31] F. Xiao, Profile-modifiable conservative transport schemes and a simple multi-integrated moment formulation for hydrodynamics, in: S. Armfield, P. Morgan, K. Srinivas (Eds.), Computational Fluid Dynamics 2002, Springer, 2003, p. 106.
[32] F. Xiao, A. Ikebata, An efficient method for capturing free boundary in multi-fluid simulations, Int. J. Numer. Methods Fluids 42 (2003) 187–210.
[33] F. Xiao, T. Yabe, Completely conservative and oscillation-less semi-Lagrangian schemes for advection transportation, J. Comput. Phys. 170 (2001) 498.
[34] F. Xiao, T. Yabe, X. Peng, H. Kobayashi, Completely conservative and oscillation-less semi-Lagrangian schemes for advection transportation, J. Geophys. Res. 107 (2002) 4609.
[35] T. Yabe, T. Aoki, A universal solver for hyperbolic-equations by cubic-polynomial interpolation. 1. One-dimensional solver, Comput. Phys. Commun. 66 (1991) 219.
[36] T. Yabe, T. Ishikawa, P.Y. Wang, T. Aoki, Y. Kadota, F. Ikeda, A universal solver for hyperbolic-equations by cubic-polynomial interpolation. 2. 2-dimensional and 3-dimensional solvers, Comput. Phys. Commun. 66 (1991) 233.
[37] T. Yabe, R. Tanaka, T. Nakamura, F. Xiao, Exactly conservative semi-Lagrangian scheme (CIP-CSL) in one dimension, Mon. Wea. Rev. 129 (2001) 332.
[38] T. Yabe, P. Wang, Unified numerical procedure for compressible and incompressible fluid, J. Phys. Soc . Jpn. 60 (1991) 2105.
[39] T. Yabe, F. Xiao, T. Utsumi, The constrained interpolation profile method for multiphase analysis, J. Comput. Phys. 169 (2001) 556.
[40] H. Yang, An artificial compression method for ENO schemes: the slope modification method, J. Comput. Phys. 89 (1990) 125.